Limited-projection-angle hybrid fluorescence molecular tomography of multiple molecules

Karin Radrich
Pouyan Mohajerani
Johanna Bussemer
Markus Schwaiger
Ambros J. Beer
Vasilis Ntziachristos

Limited-projection-angle hybrid fluorescence molecular tomography of multiple molecules

Karin Radrich,[a,b] **Pouyan Mohajerani,**[a,b] **Johanna Bussemer,**[c] **Markus Schwaiger,**[c] **Ambros J. Beer,**[c] **and Vasilis Ntziachristos**[a,b,]*

[a]Institute for Biological and Medical Imaging, Helmholtz Zentrum München, Ingolstaedter Landstrasse 1, D-85764 Neuherberg, Germany
[b]Technische Universität München, Chair for Biological Imaging, Ismaninger Strasse 22, D-81675 Munich, Germany
[c]Technische Universität München, Department of Nuclear Medicine, Ismaninger Strasse 22, D-81675 Munich, Germany

Abstract. An advantage of fluorescence methods over other imaging modalities is the ability to concurrently resolve multiple moieties using fluorochromes emitting at different spectral regions. Simultaneous imaging of spectrally separated agents is helpful in interrogating multiple functions or establishing internal controls for accurate measurements. Herein, we investigated multimoiety imaging in the context of a limited-projection-angle hybrid fluorescence molecular tomography (FMT), and x-ray computed tomography implementation and the further registration with positron emission tomography (PET) data. Multichannel FMT systems may image fluorescent probes of varying distribution patterns. Therefore, it is possible that different channels may require different use of priors and regularization parameters. We examined the performance of automatically estimating regularization factors implementing priors, using data-driven regularization specific for limited-projection-angle schemes. We were particularly interested in identifying the implementation variations between hybrid-FMT channels due to probe distribution variation. For this reason, initial validation of the data-driven algorithm on a phantom was followed by imaging different agent distributions in animals, assuming superficial and deep seated activity. We further demonstrate the benefits of combining hybrid FMT with PET to gain multiple readings on the molecular composition of disease. © *The Authors. Published by SPIE under a Creative Commons Attribution 3.0 Unported License. Distribution or reproduction of this work in whole or in part requires full attribution of the original publication, including its DOI.* [DOI: 10.1117/1.JBO.19.4 .046016]

Keywords: fluorescence molecular tomography; x-ray computed tomography; positron emission tomography; coregistration; multimodality; molecular imaging; hybrid imaging; multispectral imaging; priors; reconstruction.

Paper 140042R received Jan. 24, 2014; revised manuscript received Mar. 18, 2014; accepted for publication Mar. 25, 2014; published online Apr. 25, 2014.

1 Introduction

Fluorescence molecular tomography (FMT) reconstructs the biodistribution of fluorescent agents and reporters that enable noninvasive *in vivo* imaging of cells and cellular moieties in small animals or other tissues.[1–4] This basic ability can study disease progression or monitor therapy noninvasively *in vivo* using nonionizing energy.[4,5] An important feature of fluorescence tomography is the ability to visualize different functional or molecular parameters in the same animal, using fluorochromes emitting at different spectral bands. One advantage of approaches like this is the creation of internal controls using, e.g., an active and an inactive form of an agent, each labeled with a different fluorochrome.[6,7] In this example, biodistribution and delivery of the agent can be separated by active targeting on the same animal by comparing the images at the two fluorescence channels. Alternatively, different contrast mechanisms can be concurrently studied, e.g., the relative expression of different receptors or the relative concentrations of different types of cells.

A complication of FMT imaging has been the ill-posed nature of the inversion problem[8–10] which limits the resolution and the overall quantification ability of the method. Correspondingly, different regularization schemes have been proposed, e.g., the frequently employed Tikhonov regularization,[9,11,12]

to improve the accuracy. Implementations that combine an anatomical imaging modality with FMT have also been proposed to improve the inversion problem using anatomical information in the inversion scheme.[13–17] Anatomical information can be employed in the forward model of photon propagation to include realistic internal boundaries of the tissue examined.[18,19] They can be further inserted in the inversion problem in the form of priors to improve the regularization of the problem, typically in a segment wise fashion with each segment corresponding to a different anatomical region.[20,21]

Hybrid FMT x-ray computed tomography (XCT) imaging geometries collecting tomographic data over 360-deg projections have been reported[22–24] and demonstrated significant improvements in imaging performance compared to stand-alone FMT. However, these systems require dedicated hardware and are expensive. Alternatively, the registration of FMT data acquired in the planar geometry has been achieved using a rigid holder to image animals under identical placement by different modalities.[25] These systems have also demonstrated improvements over stand-alone systems and offer a practical implementation that can also capitalize on the placement of several stand-alone FMT and x-ray systems worldwide. A particular aspect of the planar geometry is that it typically requires shorter acquisition times compared to 360-deg devices, which accelerates experimental time and reduces animal stress.

A next important step in the progress of limited-projection-angle hybrid FMT approaches is the development of multispectral schemes that capitalize on the unique ability of the hybrid

*Address all correspondence to: Vasilis Ntziachristos, E-mail: v.ntziachristos@tum.de

optical method to simultaneously image several targeted agents at higher imaging accuracy than stand-alone FMT systems. Dual-wavelength concepts based on the combination of one targeted and one untargeted probe have been introduced for 360-deg FMT systems.[7,26] Instead, we interrogated, herein, the performance of multispectral methods employing limited-projection-angle FMT setups, which are more widely disseminated than 360-deg systems. Limited-projection-angle FMT offers implementation simplicity, as it does not require rotating gantries but offers a subset of the information available to 360-deg systems. We particularly aimed at providing a framework for reconstructions of multiple biological parameters that are independent of the user input. This could enable nonbiased imaging of multiple fluorochromes in the same animal and lead toward simultaneous multispectral investigations of the biodistribution of different molecules involved in disease progression or treatment efficacy.

Multiparameter imaging has been successfully implemented in optical microscopy[27] or epi-illumination methods.[28] The importance of multiparameter investigation is also reflected in the emergence of new research fields such as systems biology, which emphasizes the ability to interrogate network properties and interactions of at least a few hundreds of proteins and genes. This has driven the development of new fluorescence dyes and probes, which allow imaging at multiple wavelengths.[27,29] Complementing traditional molecular biology methods with the noninvasive acquisition of multimolecular information is highly desirable as a unique method that can offer insight into dynamic processes in unperturbed biological tissues. Correspondingly, hybrid FMT reconstructions implemented using automatically computed priors have the potential to deliver better accuracy in volumetric multiwavelength imaging, complementing multiwavelength (multispectral) imaging strategies considered in two-dimensional surface weighted epi-illumination mode.[28–30]

The study design, herein, had two major goals. The first was to investigate the previously unexplored ability and relative accuracy by which two different fluorescent agents can be resolved in the same mouse simultaneously, when using hybrid implementations in limited-projection-angle FMT using priors. For this purpose, we adapted a previously described method implementing spatially varying regularization,[31] which was initially developed based on 360-deg FMT data, and optimized it for limited-projection-angle FMT-XCT. Our particular interest, herein, was to evaluate whether and how the automatic computation of regularization factors could be translated to limited-projection-angle FMT reconstructions. Therefore, we characterized different regularization factor computation results based on varying regularization parameters used, and offer improved reconstruction metrics for data driven a priori regularization. In contrast to manual factor selection as applied in our previous study,[25] this approach solely relies on automatically computed regularization factors and therefore enables independent reconstruction of different fluorescent probes.

The second goal was to demonstrate an extension of the application of hybrid FMT-XCT using the XCT to further register hybrid FMT findings with those from another molecular imaging modality, i.e., positron emission tomography (PET). This second goal can lead to the integration of optical contrast with that of other imaging modalities, yielding an information dataset that is of increased descriptive ability as to disease parameters. In the particular example, herein, we combined imaging of

tumor vascularization or vascular endothelial growth factor (VEGF) expression, $\alpha_v\beta_3$-integrin overexpression and tumor metabolism using coregistered [18F]-FDG-PET and FMT-XCT, providing multiparametric datasets.

By this experimental study, we provide a methodological framework for multimolecular *in vivo* investigations. We discuss the obvious extension of this work by employing a larger number of fluorescent agents at different spectral bands and the possibility of coregistration with a larger number of imaging modalities.

2 Methods

2.1 Limited-Projection-Angle FMT-XCT Acquisition and Coregistration

Acquisition and coregistration of FMT and XCT datasets were performed as previously described in Ref. 25. In brief, anesthetized mice were placed in an imaging cartridge consisting of two transparent parallel plates. These served the purpose of immobilizing the mice during the different measurement steps and for translation between imaging devices. Also, it provided a common coordinate system that could be used for coregistration of all datasets due to its rigid shape.

FMT images were acquired in transillumination mode using a commercially available limited-projection-angle FMT device (FMT 2500, VisEn Medical, Woburn, Massachusetts—now PerkinElmer) with two channels at 680/700 and 750/770 nm excitation/emission wavelength, respectively. The acquisition time for each channel was 5 to 10 min.

XCT data were acquired using a micro-PET-XCT device (Inveon, Siemens Preclinical Solutions, Knoxville, Tennessee) in 10 to 15 min and automatically reconstructed by the manufacturer's software. The reconstructed datasets were exported in digital imaging and communication in medicine (DICOM) format to be coregistered with the FMT data. Segmentation of bones, lungs, and heart was performed as previously described.[25,32] For the subcutaneous tumor mice, an additional segmentation of the tumor area was performed. This area was selected manually based on the XCT images.

2.2 PET Acquisition, Coregistration, and Reconstruction

PET data were acquired using the same micro-PET-XCT device as for XCT data acquisition. After XCT imaging, the mouse was automatically passed on into the PET device. [18F]-FDG-PET acquisition took around 8 min.

Reconstruction of PET data was realized by the manufacturer's software and DICOM images were exported for coregistration to FMT-XCT data. Since PET and XCT data were acquired with a hybrid device, coordinates for coregistration of both datasets were given by the device manufacturer, and coregistration to FMT-XCT reconstructions was therefore straightforward.

2.3 FMT-XCT Reconstruction

The reconstruction process was performed as described in Ref. 25, except that automatic schemes for spatially varying regularization were researched and employed here instead of manually chosen priors.

Briefly, photon propagation was modeled based on a solution of the diffusion equation, implemented using a finite element

solver.[22] For a set of measurements between multiple source-detector pairs contained in vector y and obtained from an unknown fluorescence distribution x, the solver calculated a weight matrix leading to a linear matrix equation

$$y = Wx. \tag{1}$$

Each row in W contains the relative contribution of all different voxels in the image x for a single source-detector measurement. Correspondingly, different rows contain a similar calculation for each source-detector pair measurement.

The inversion of Eq. (1) leads to an ill-posed problem that needs regularization of the residual norm, which is often realized by a Tikhonov type regularization matrix.[9,11] It is known that the reconstruction of x can be improved by integrating anatomical information in the regularization term of the inverse problem.[20,25] This results in the following expression:

$$X = \mathrm{argmin}(\|Wx - y\|_2^2 + \lambda^2 \|Lx\|_2^2), \tag{2}$$

where L is the regularization matrix which contains in this case different values for different tissue segments in its diagonal, henceforth denoted as regularization factors, instead of being the identity matrix as typical in the conventional Tikhonov regularization. λ represents the regularization parameter that determines the influence of the second term, and therefore in our case of the respective *a priori* knowledge, on the minimization problem. X is the result of the reconstructed fluorescence distribution.

2.4 Automatic Estimation of Regularization Factors for Reconstructions Using Priors

A data-driven two-step inversion method was previously proposed in the context of 360-deg systems[21,31] for automatically estimating spatially varying regularization factors in the L-matrix, employed to establish priors in Eq. (2). The two-step inversion method consists of a first inversion step, performed using anatomical information as prior information in the forward model and employing Eq. (2) with $L = I$ (I being the identity matrix) to derive the relative fluorescence strengths per segment. Regularization factors for each segment are then estimated from reconstructed intensity values in the different tissue segments; typically, proportionally to the calculated mean signal intensity per segment. The second inversion step incorporates these segment-specific regularization factors into the diagonal of the L-matrix in order to achieve spatially varying regularization in combination with an adequate regularization parameter λ. The advantage of the two-step data-driven approach is that it is free of user-based assumptions or heuristic selection of regularization factors.

Stand-alone FMT reconstructions based on limited-projection-angle (planar) geometries tend to have surface artifacts.[31] This effect is more pronounced as the number of projections decreases.[33] In addition, limited projections limit the resolution achieved along the projection axis.[34] Our approach, herein, consisted of investigating whether automatically computed regularization factors can lead to improvements in these artifacts and yield more accurate images. For this purpose, we examined how different regularization parameters λ would influence the computation of regularization factors in the step 1 inversion. Our objective was to find an ideal λ for the automatic estimation

of regularization factors for the step 2 inversion. This was initially tested on phantom data containing fluorescent insertions.

During the step 1 inversion described above, Tikhonov reconstruction using the identity matrix was performed and an initial regularization parameter was chosen by L-curve analysis at the L-curve corner.[35] Subsequently, we increased the value of λ until we created an over-regularized state represented by smoothing the entire reconstruction toward a single bright lesion in the middle of the phantom. The motivation for this L-curve analysis was to find a value for λ where the regularization is high enough to suppress surface artifacts, but still enable a representative overall fluorescence distribution. The best λ value identified in this process was then used in the step 1 inversion to derive segment-specific regularization factors, the latter employed in the L-matrix of the step 2 inversion. The segment-specific regularization factors were determined by computing the mean reconstructed intensity I_{seg} per segment

$$I_{\mathrm{seg}}(\lambda) = \frac{\sum_{\mathrm{seg}} x_{\mathrm{recon}}(\lambda)}{N_{\mathrm{voxel,seg}}}, \tag{3}$$

to be the sum of the reconstructed fluorescence x_{recon} in each segment divided by the number of voxels in this segment $N_{\mathrm{voxel,seg}}$. The I_{seg} values were then normalized so that the segment with the highest I_{seg} value was attributed the value 1 in the L-matrix (during the step 2 inversion), the segment with the lowest I_{seg} value was attributed the value of 3, and all other segments were regularized with a value between 1 and 3 proportionally to their I_{seg} value. This allocation of L-matrix regularization factors is, therefore, a variation of the method presented by Hyde et al.[31] An approach that has been validated in the past and confirmed to yield optimal results.[21,25]

2.5 Phantom Characteristics

The phantoms and corresponding acquisition data employed in this study have been reported in Ref. 25. The phantoms were composed of a mixture of intralipid, ink, agar, and water according to the known spectral properties of ink and published scattering properties of intralipid, in order to attain tissue properties of $\mu_s{}' = 12\ \mathrm{cm}^{-1}$ and $\mu_a = 0.2\ \mathrm{cm}^{-1}$. They were shaped to semicylinders resembling the shape of a mouse torso, with a maximal diameter of 30 mm. Two tubes filled with a fluorescence dye with the peak excitation at 679 nm and peak emission at 702 nm (Alexa Fluor 680, Life Technologies Ltd, Paisley, UK) were inserted into the phantom to mimic fluorescently labeled tumors.

The phantom data were used to develop and test the automatic regularization factor estimation from coregistered limited-projection-angle FMT-XCT on clearly defined and well-known tissue before moving on to the more heterogeneous mouse models where the fluorescence biodistribution is typically unknown prior to *ex vivo* validation.

2.6 Animal Studies

Three mouse models were employed in this study, two for studying superficial tumors and one exhibiting deeper-seated tumors. Optical signals attenuate nonlinearly with the source depth. Consequently, the selection of different depths is important in the investigations of optical imaging to examine the ability of the method to reliably perform as a function of depth.

Deep-seated tumors were investigated using a transgenic mouse model spontaneously developing tumors in the lung (Kras, Ref. 36). Mice at the age of approximately 15–18 weeks were injected intravenously before imaging with, respectively, 2 nmol of two different fluorescence probes, one targeting $\alpha_v\beta_3$-integrins (IntegriSense680, Perkin Elmer, Waltham, Massachusetts) and a blood-pool agent (AngioSense750 Perkin Elmer, Waltham, Massachusetts). The excitation/emission maxima of IntegriSense680 and AngioSense750 are approximately at 680/705 nm and 750/770 nm, respectively. Angio-Sense can be used in oncology to study angiogenesis and was, therefore, chosen to provide information on vascularization and perfusion, in addition to the molecular information granted by the $\alpha_v\beta_3$-integrin overexpression. AngioSense was injected in different mice both 1.5 and 24 h prior to imaging but did not show significant biodistribution differences between these two time points as confirmed by *ex vivo* validation studies. We hence only show, herein, results from a mouse injected 24 h prior to FMT-XCT measurements, i.e., at the same time point for which IntegriSense data was also acquired. This study examined, therefore, a physiological parameter (vascularization/perfusion) and a molecular parameter ($\alpha_v\beta_3$-integrin overexpression).

The second mouse model was a xenograft breast cancer model. We subcutaneously injected Balb/C nude mice with 10^6 4T1 cells in the neck region and let the tumor grow for 10 days. Twenty-fours hours prior to imaging, mice were intravenously administered scVEGF/Cy (SibTech Inc., Brookfield, Connecticut), a fluorescence agent binding to VEGF receptor 2 (VEGFR-2) and emitting at around 700 nm. This agent was employed to study the ability to visualize a second molecular target in one channel, whereby the second channel again imaged IntegriSense750. In this way, we could examine the relative distribution patterns of VEGFR-2 and $\alpha_v\beta_3$-integrin.

The third mouse model was employed to demonstrate the capacity of hybrid FMT-XCT and to combine the findings with results from PET imaging. In this pilot study, 6×10^6 Lewis lung carcinoma (LLC) cells were injected subcutaneously in the right shoulder region and 4×10^6 cells in the left shoulder region of a nude mouse. The tumors were allowed to grow for 9 days. Twenty-four hours before FMT-XCT imaging, the mice was injected with IntegriSense680. Additionally, 45 min before PET imaging the mice were injected with approximately 13 MBq of [^{18}F]-FDG tracer.

For imaging, mice were anesthetized (Isoflurane 2%, O_2 0.9 L/min), placed in an imaging cassette, and consecutively imaged by XCT, PET (only for LLC mice), and FMT. After imaging, they were euthanized and frozen at $-80°C$ for *ex vivo* validation.

2.7 Imaging Performance Validation

For validation, the frozen mice were cryosectioned in a cryotome (CM 1950, Leica Microsystems GmbH, Wetzlar, Germany). During slicing, we employed an imaging system[37] to acquire images of the real fluorescence distribution in every tissue slice at both wavelengths to be compared to our *in vivo* results. Images were acquired every 200 μm.

We compared the relative contrast of the fluorescence strength between tumors and different tissues *in vivo* and *ex vivo* in order to assess the performance of our reconstruction method. For that, we computed the relative contrast $C_{T1,T2}$ between any two regions $T1$ and $T2$ analogously to standard contrast-to-noise calculations as:

$$C_{T1,T2} = \frac{\mu_{T1} - \mu_{T2}}{\frac{1}{n}\sqrt{\sum_n \sigma_{Tn}}}, \qquad (4)$$

where μ_{T1} represents the mean signal intensity in one region (for instance tumor) and μ_{T2} represents the mean signal intensity in a second region (for instance muscle), n is the number of different regions (or segments) in a mouse or phantom, and σ_{Tn} is the standard deviation of the signal in the n'th region. $C_{T1,T2}$ can become negative if the mean signal intensity in $T2$ is higher than in $T1$, i.e., $\mu_{T1} < \mu_{T2}$. For $|C_{T1,T2}| \leq 1$, the contrast is not distinguishable from the noise level in the images. For good contrast, we expect $|C_{T1,T2}| \gg 1$.

For Kras mice, we chose regions of interest in the tumor, muscle, lung, and heart and for 4T1 mice, we chose ROIs in the center and margin of the tumor, as well as in muscle tissue near the tumor. We also quantified the relative contrast reconstructed *in vivo* in each of the whole tissue segments.

The accuracy of the localization of the reconstructed fluorescence signal in the phantom was evaluated as a function of the regularization parameter λ used for respective regularization factor computation. To assess the reconstruction error, we computed the percentage of the reconstructed signal in an area delineated by a distance of 2 mm around the fluorescence tubes (as described in Ref. 25). We further evaluated the accuracy of the localization in Kras, 4T1, and LLC experiments based on intensity profiles through the *in vivo* and *ex vivo* images. The threshold set for assuming that a fluorescence signal originates from a location of true probe accumulation was set as the mean signal intensity in the entire mouse plus two standard deviations of background noise (as previously described in Ref. 38).

3 Results

3.1 Evaluation of Regularization Factor Estimation

Figure 1(a) depicts four phantom reconstructions with different values of λ using standard Tikhonov regularization, and the corresponding L-curve. The shown representative values of λ_n included λ_1 and its 2^{n-1} multiples ($\lambda_2 \approx \lambda_1 \cdot 2^1$; $\lambda_3 \approx \lambda_1 \cdot 2^2$; $\lambda_4 \approx \lambda_1 \cdot 2^3$). Reconstruction for λ_1 shows an elongated appearance of the circular objects (fluorescent tubes) with the peak intensity biased toward the surface. As the λ values increase from λ_1 to λ_4, the reconstructed image appears more diffusive in nature but the elongation is retained, due to the limited angle projection data collected by the system. Figure 1(b) lists the values of λ_1 to λ_6 in its rows and the corresponding regularization factors for the two tubes and the background in its columns. The left tube was assigned the lowest regularization factor of 1 for all cases while the regularization factor for the right tube changed with λ. The step 2 reconstructions resulting from using the regularization factors computed with λ_1 to λ_6 are evaluated in the rightmost two columns. The normalized relative contrast (i.e., contrast values divided by the largest contrast value, which was 17.5) between right tube and tissue and the percentage of reconstructed signal lying up to 2 mm outside the tube margin are given. Figure 1(c) shows the computed regularization factors for the right tube as a function of all λ's starting at the L-curve corner with λ_1 as a continuous line. We observed that the regularization factors between λ_1 and λ_3 are in a similar value range, with a local minimum at λ_3, but rise quickly for higher values of λ. The dashed line shows the change of the normalized relative contrast in the right tube after step 2 inversion as
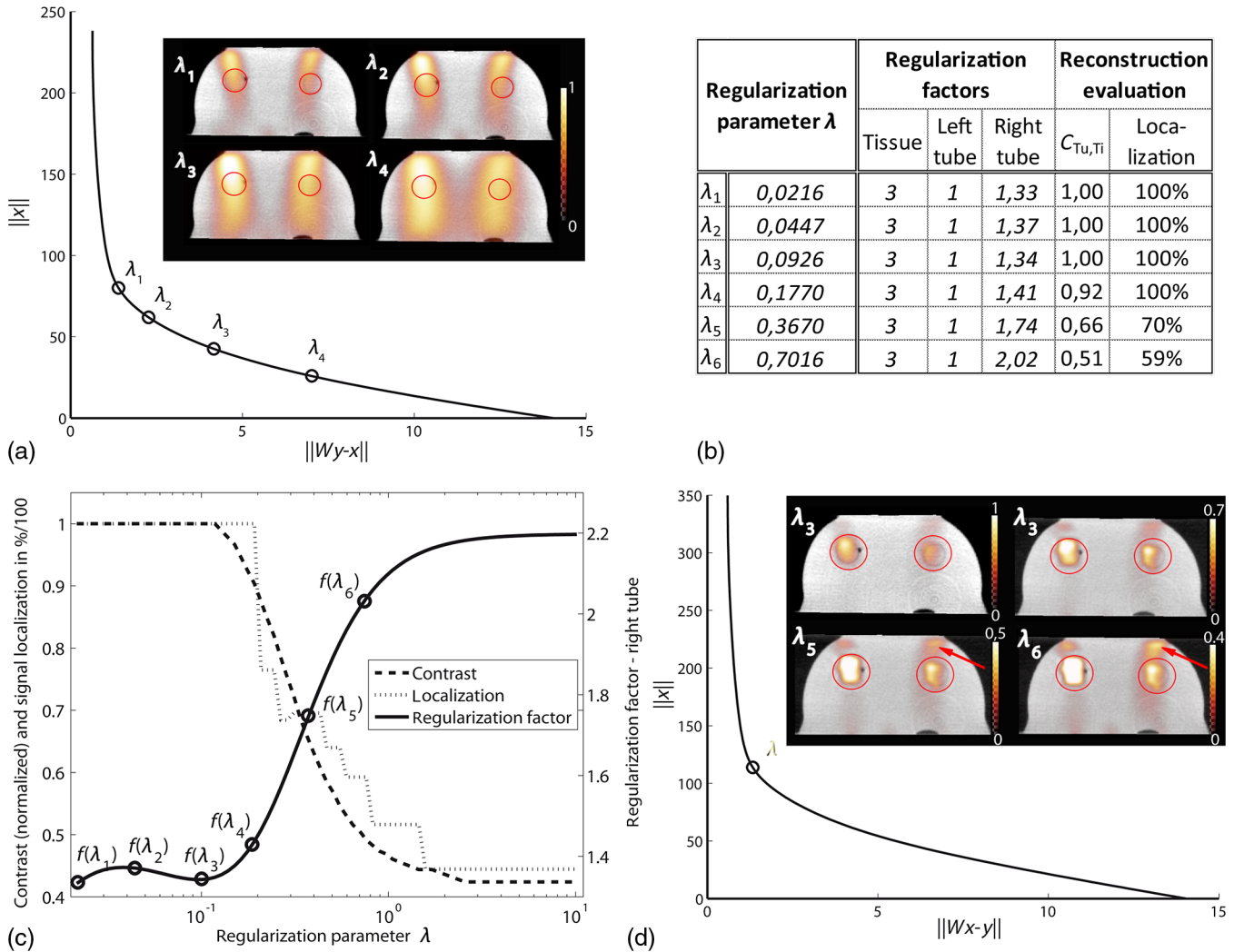
(a)

(b)

Regularization parameter λ		Regularization factors			Reconstruction evaluation	
		Tissue	Left tube	Right tube	$C_{Tu,Ti}$	Localization
λ_1	0,0216	3	1	1,33	1,00	100%
λ_2	0,0447	3	1	1,37	1,00	100%
λ_3	0,0926	3	1	1,34	1,00	100%
λ_4	0,1770	3	1	1,41	0,92	100%
λ_5	0,3670	3	1	1,74	0,66	70%
λ_6	0,7016	3	1	2,02	0,51	59%

(c)

(d)

Fig. 1 (a) Tikhonov reconstruction (step 1 inversion) of fluorescence inclusions (red circles) in a tissue-mimicking phantom for different regularization parameters λ, marked on the corresponding L-curve. (b) Regularization factors computed from the respective reconstructions using six different λ values and resulting contrast ratios and localization accuracy. (c) Computed regularization factor of the right tube as a function of λ (continuous line), normalized contrast between right tube and tissue (dashed line), and percentage of signal localized within 2-mm distance of the right tube (dotted line). (d) Reconstructions using regularization factors calculated for λ_3, λ_5, and λ_6 (step 2 inversion). The red circles represent the area for localization evaluation defined by the tube radius +2 mm. The chosen regularization parameter for step 2 lies near the point of maximum curvature of the step 2 L-curve, at the L-curve corner.

a function of the used regularization parameter for regularization factor estimation. The dotted line depicts the change of the percentage of the reconstructed signal lying within a distance of 2 mm from the tube. Figure 1(d) finally shows the examples for the fluorescence distribution after step 2 inversion using the regularization factors computed from step 1 inversion with λ_3, λ_5, and λ_6. The results from Figs. 1(b) and 1(c) suggest that the relative contrast decreases for regularization factors computed with $\lambda > \lambda_3$ and the localization accuracy for $\lambda > \lambda_4$. This becomes obvious in the presented examples. The top two phantom slices show the same reconstruction with regularization factors computed with λ_3, but with different scaling to bring out the maximum signal in the right tube. The two reconstructions on the bottom of Fig. 1(d) for λ_5 and λ_6 are also scaled to the maximum value of the signal in the right tube.

Here, it becomes obvious that similarly high signals are also reconstructed outside the tube area (arrows). Red circles highlight the region that was used for the localization evaluation, i.e., tube radius +2 mm. The independent regularization parameter λ used in step 2 was chosen to be the commonly used optimal solution lying at the L-curve corner. In contrast to the phantom reconstruction using priors shown in Ref. 25 where the regularization factors were manually set, the result in Fig. 1(d) was achieved by automatic computation based on experimentally determined regularization factors.

3.2 Dual-Wavelength Experiments

Table 1 lists the computed regularization factors after step 1 inversion for both Kras and 4T1 mouse models at the two

employed wavelengths and represents the mean reconstructed fluorescence strength per λ (columns) and segment (rows).

For Kras mice, step 1 inversion with λ_1 suggests that the fluorescent probe uptake at both wavelengths was highest in the bones. This would result in a segment-specific regularization factor of 1 in the L-matrix of Eq. (2), representing the step 2 inversion. The other segment-specific entries into the L-matrix, i.e., for tissue, lung, and heart, at 680 nm would for instance be 1.6, 2.21, and 3, respectively. The computation of these segment-specific regularization factors changes as a function of increasing λ, as can be seen in Table 1 for the values computed with λ_2 and λ_3. In contrast to the results obtained with λ_1, step 1 inversion with λ_3 suggests that the highest fluorescence probe uptake at 680 nm is in the lung. In this case, the elements of the L-matrix corresponding to the lung segment would be assigned a value of 1.

Figure 2 shows the results after step 2 inversion of the Kras mouse model using the respective regularization factors from Table 1 for λ_3. Figure 2(a) depicts the two *in vivo* reconstruction slices at different locations in the chest of the mouse and Fig. 2(b) contains the corresponding *ex vivo* cryosections for validation. An example for the choice of regions of interest for the determination of the relative contrast between tissues is given in the top *in vivo* and *ex vivo* slices by dashed white ellipses for tumor (t), muscle (m), lung (l), and heart (h). The bottom slice in Fig. 1(a) additionally shows the segmentation of lung and heart in the *in vivo* data as white dashed contour lines. Figure 2(c) depicts a three-dimensional (3-D) rendered image of the whole reconstructed volume. Here, the lung is shown in transparent light yellow in order to allow the evaluation of the location of the reconstructed fluorescence distribution. In all panels of Fig. 2, the cyan signal represents the distribution of IntegriSense680 and magenta the distribution of AngioSense750. Cyan arrows highlight the tumors and magenta arrows the heart. A clear difference in the biodistribution of the two probes is observable in the *ex vivo* slices. This is reflected in the *in vivo* reconstruction, where IntegriSense680 is mainly reconstructed in the tumor area and AngioSense750 is more broadly distributed in the lung and heart area.

Figure 2(d) shows the normalized intensity profiles through the dashed straight white lines in the *in vivo* and *ex vivo* slices in Figs. 2(a) and 2(b). Dashed lines in the graph represent *in vivo* and continuous lines *ex vivo* data. An arrow highlights the position of the biggest tumor in the *ex vivo* slice [Fig. 2(b)] and the graph to facilitate correlation of corresponding data points. The *ex vivo* intensity profile shows high IntegriSense680 uptake in the tumor compared to the surrounding lung as well as to heart and the other tissue. *Ex vivo* fluorescence distribution of AngioSense750 in tumor, lung, and heart on the contrary is of a similar intensity level. The *in vivo* profiles qualitatively mirror the *ex vivo* profiles when it comes to recovering the highest fluorescence peaks. For AngioSense750, though, a descent between tumor and heart area can be observed that is higher than observable in the *ex vivo* validation slices. We further examined the agreement between *in vivo* reconstructions and *ex vivo* cryosections by comparing the relative contrast between tissue segments and between selected regions of interest, as described in Sec. 2. Table 2 lists these values where rows contain the different contrast ratios, columns the respective fluorescent probe. The compared tissues are given in the "Regions" column, where the first tissue goes as μ_{T1} and the second tissue as μ_{T2} into Eq. (4), respectively. Highest whole segment contrast for IntegriSense680 was obtained for the lung region and accordingly for ROIs in the tumor, both *in vivo* and *ex vivo*. Although the contrast between the whole lung and other tissues is still rather low due to the contribution of both diseased and normal lung tissue, contrast ratios rise significantly when focusing on the contribution of the tumors alone. For AngioSense750, the small absolute value of the lung/heart contrast ratio indicates little contrast between those segments. Similarly high values were also obtained when comparing localized tumor signals to both heart and lung.

Figure 3 shows the results after step 2 inversion of the 4T1 mouse model using the respective regularization factors listed in Table 1 for λ_3. Figure 3(a) depicts two *in vivo* reconstruction slices at different locations in the neck/shoulder region of the mouse and Fig. 3(b) contains the corresponding *ex vivo* cryosections for validation. An example for the choice of ROIs is given

Table 1 Regularization factors computed for different values of λ after Tikhonov reconstruction of Kras and 4T1 mouse models. Columns contain values for each respective λ and rows contain values for each respective segment. For both wavelengths, the model-specific segments are allocated a factor between 1 and 3 representing the mean reconstructed fluorescence strength in this segment. A value of 1 means highest fluorescence signal, a value of 3 lowest fluorescence signal.

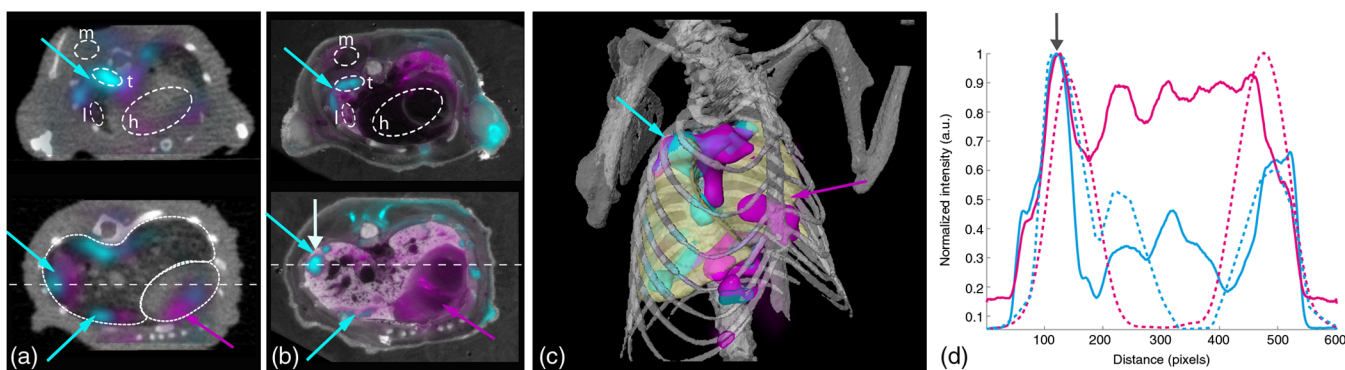| Wavelength		KRas				4T1		
	Segment	λ_1	λ_2	λ_3	Segment	λ_1	λ_2	λ_3
680	Tissue	1.60	2.85	3.00	Tissue	2.89	3.00	3.00
	Bone	1.00	1.00	2.10	Bone	3.00	2.54	1.78
	Lung	2.21	1.41	1.00	Tumor	1.00	1.00	1.00
	Heart	3.00	3.00	1.77				
750	Tissue	1.55	3.00	3.00	Tissue	3.00	3.00	3.00
	Bone	1.00	1.49	1.92	Bone	2.94	2.76	2.51
	Lung	3.00	2.67	1.09	Tumor	1.00	1.00	1.00
	Heart	2.08	1.00	1.00				

Fig. 2 Reconstruction of Kras tumor model using two different fluorescence probes and the two-step inversion approach. (a) Overlay of two representative slices of *in vivo* reconstructions of IntegriSense680 (cyan) and AngioSense750 (magenta) of the Kras mouse. Regions of interest in tumor (t), lung (l), muscle (m), and heart (h) for contrast evaluation are shown in the top slice. White dashed contours in the bottom slice show the segmentation of lung and heart. (b) Overlay of the corresponding fluorescence cryosection images. (c) Three-dimensional (3-D) representation of the reconstructions throughout the volume. (d) Intensity profiles through the straight white dashed lines in (a) and (b) of IntegriSense680 (cyan) and AngioSense750 (magenta) for *in vivo* (dashed lines) and *ex vivo* (continuous lines), respectively. (3-D rendering was implemented using AMIRA software).

in the top *in vivo* and *ex vivo* slices by dashed white ellipses for tumor margin (t_m), tumor center (t_c), and muscle (m). The bottom slice in Fig. 3(a) shows the contour of the tumor segment used for *in vivo* reconstruction. In all panels of Fig. 3, the cyan signal represents the distribution of scVEGF/Cy and magenta the distribution of IntegriSense750. Both *in vivo* and *ex vivo* slices show IntegriSense750 accumulation in the center of the tumor whereas scVEGF/Cy is accumulated at the tumor margin (cyan arrows). Figure 3(c) depicts a 3-D rendered image of the reconstructed fluorescence at both wavelengths. The reconstruction of scVEGF/Cy uptake throughout the mouse is equivalent as for the single slices shown in Fig. 3(a), namely on the tumor boundary. This probe mainly accumulates in the margins (note the donut shape of the reconstruction) and IntegriSense750 is in its center, with some overlap of both probes in the peripheral regions of the tumor.

The same quantitative analysis as for the Kras model was performed on the 4T1 model. Figure 3(d) depicts the intensity profiles through the dashed white straight lines in *ex vivo* and *in vivo* slices in Figs. 3(a) and 3(b). The graph shows in cyan the normalized intensity of scVEGF/Cy emission and in magenta the normalized intensity of IntegriSense750 emission. Dashed lines represent the *in vivo* and continuous lines *ex vivo* data. An arrow highlights the position of the tumor boundary in the *ex vivo* slice [Fig. 3(b)] and the graph to facilitate correlation

of corresponding data points. The intensity profile of scVEGF/Cy shows the highest intensities at the tumor margins while the highest peak for IntegriSense750 is in the tumor center, both for *ex vivo* and *in vivo* data. Contrast ratios for the whole tissue segments and for the selected regions of interest are listed in Table 3. The whole segment contrast ratios show that both probes are accumulated in the tumor segment. Contrast between ROIs in the tumor center and margin furthermore confirm the exact localization of the accumulation of each probe, i.e., in the margin for scVEGF/Cy and in the center for IntegriSense 750. *In vivo* and *ex vivo* contrast ratios were in qualitative agreement, i.e., highest contrast was achieved for margin/tissue for scVEGF/Cy and center/tissue in both reconstructions and cryosections.

3.3 FMT-XCT-PET Study

Figure 4 shows the reconstruction results of the LLC mouse model including FMT, XCT, and PET data. In this case, the expression of $\alpha_v\beta_3$-integrin was tracked with an optical probe and metabolic activity with an [18F]-FDG PET radiotracer. The reconstruction of IntegriSense680 was performed analogously to the phantom, Kras, and 4T1 studies, i.e., using $\lambda_3 \approx 2^2 \cdot \lambda_1$, with λ_1 being the regularization parameter at the L-curve corner of the step 1 regularization of the LLC mouse.

Table 2 Comparison of *in vivo* and *ex vivo* contrast ratios in Kras mouse model. Left: Computed relative contrast for whole segments for both wavelengths. Right: Relative contrast of model specific regions of interest. For Kras: tumor-to-lung, tumor-to-muscle, and tumor-to-heart contrast.

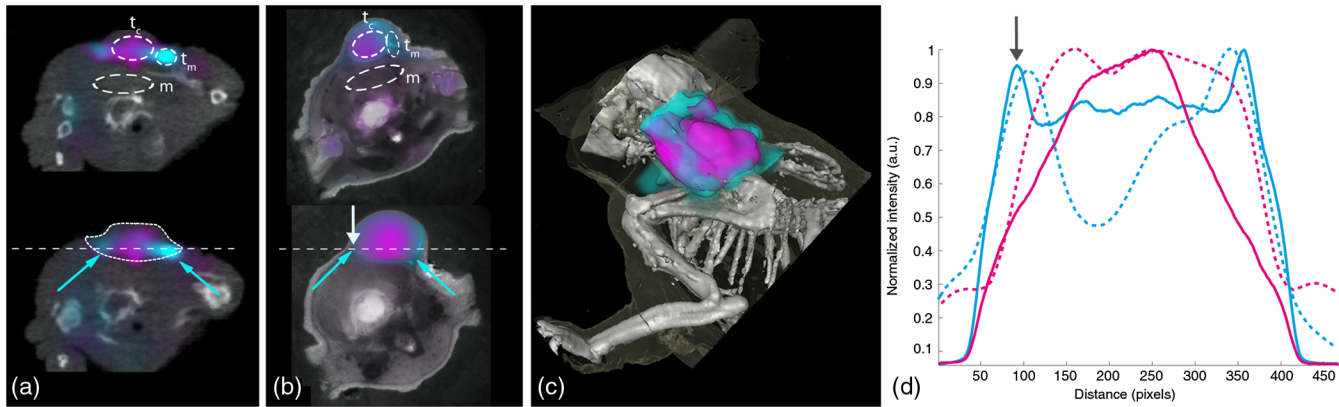| Kras—relative contrast (whole segments)			Kras—relative contrast (ROI)				
	In vivo			*In vivo*		*Ex vivo*	
Regions	IS680	AS750	Regions	IS680	AS750	IS680	AS750
Lung/Tissue	2.47	1.24	Tumor/Lung	10.81	5.69	24.43	3.98
Lung/Bones	1.42	0.18	Tumor/Muscle	11.60	6.42	20.75	11.01
Lung/Heart	1.85	−0.37	Tumor/Heart	12.43	3.89	34.78	5.82

Fig. 3 Reconstruction of 4T1 tumor model using two different fluorescence probes and the two-step inversion approach. (a) Overlay of scVEGF/Cy (cyan) and IntegriSense750 (magenta) in two representative slices from *in vivo* reconstruction. Regions of interest in tumor margin (t_m), tumor center (t_c), and muscle (m) for contrast evaluation are shown in the top slice. The white dashed contour in the bottom slice shows the segmentation of the tumor. (b) Overlay of the corresponding fluorescence cryosection images. (c) 3-D representation of the reconstructions throughout the volume. (d) Intensity profiles through the straight white dashed lines in (a) and (b) of scVEGF/Cy (cyan) and IntegriSense750 (magenta) for *in vivo* (dashed lines) and *ex vivo* (continuous lines) data, respectively. (3-D rendering was implemented using AMIRA software).

Figure 4(a) depicts the different distribution of the two tracers, the *in vivo* reconstruction of IntegriSense680 being shown in orange and the [18F]-FDG-PET tracer in green. Figure 4(b) shows the *ex vivo* validation of the optical probe distribution where the fluorescence signal is shown as contrast-enhanced orange overlay on a white light image. Figure 4(c) visualizes the 3-D distribution of IntegriSense680 and [18F]-FDG reconstructions and Fig. 4(d) indicates the locations of the subcutaneous LLC tumors on the 3-D rendered mouse skin by orange arrows. Figure 4(e) depicts the normalized intensity profiles through the white dashed lines in Figs. 4(a) and 4(b). Continuous curves represent the profiles through line 1 and dashed curves through line 2. The graph shows in orange the normalized intensity of IntegriSense680 emission in the *ex vivo* slice [Fig. 1(b)], in yellow the *in vivo* IntegriSense680 reconstruction [Fig. 1(a)], and in green the normalized intensity of [18F]-FDG. A gray arrow highlights the position of the left tumor in the *ex vivo* slice [Fig. 4(b)] and the graph to facilitate correlation of corresponding data points.

We observed that IntegriSense680 is only reconstructed in the tumor area, in accordance with the *ex vivo* slice image. The size of the left tumor, though, was overestimated and a slight dislocation between *ex vivo* and *in vivo* fluorescence

locations could be observed. As can be expected, FDG (green) shows the metabolic activity and is therefore not only distributed in the tumors but also in heart and brain. An additional aggregation of FDG can be observed, though, between the two tumors, as highlighted by green arrows in Figs. 4(a), 4(c), and 4(e). This is neither visible after IntegriSense680 reconstruction nor is a third tumor distinguishable in the *ex vivo* slice.

4 Discussion

Multichannel imaging is generally available to only a few imaging modalities, most notably optical,[28] and optoacoustic imaging.[39] The guiding force in this study was to develop multispectral and multimodality FMT using a limited-projection-angle hybrid implementation in combination with XCT. Particularly, we aimed at enabling simultaneous investigation of multiple molecules using limited-projection-angle, hybrid FMT-XCT, a capacity not documented before in the literature. Contrary to assuming that imaging two targets would only be a matter of adding an additional filter and a light source to the previously developed limited-projection-angle FMT-XCT system,[25] the study, herein, instead focused on adapting a spatially varying regularization inversion method,[31] previously described

Table 3 Comparison of *in vivo* and *ex vivo* contrast ratios in 4T1 mouse model. Left: Computed relative contrast for whole segments for both wavelengths. Right: Relative contrast of model specific regions of interest. For 4T1: tumor-margin-to-center, tumor-margin-to-tissue, and tumor-center-to-tissue ratios.

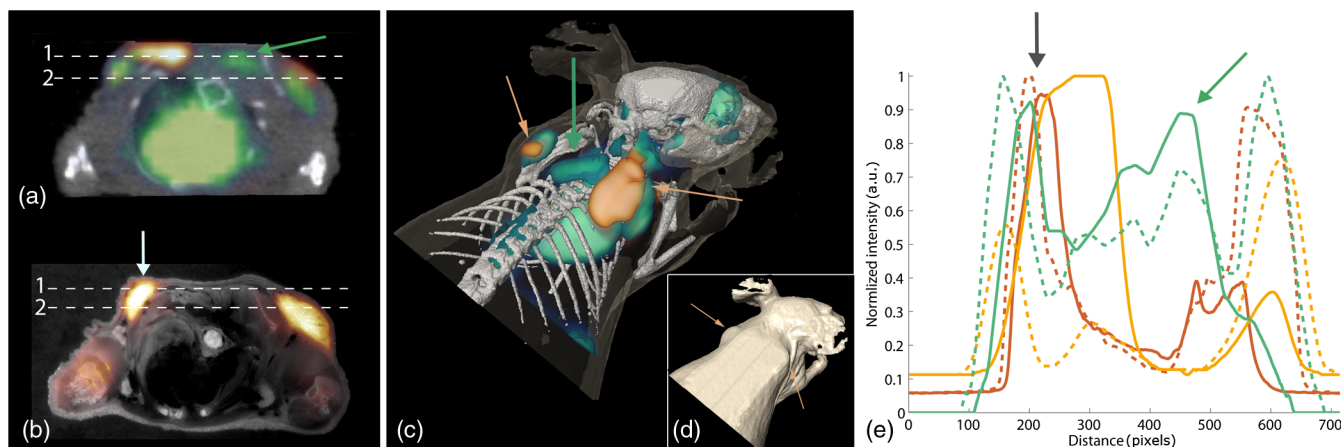| 4T1—relative contrast (whole segments)			4T1—relative contrast (ROI)				
	In vivo			*In vivo*		*Ex vivo*	
Ratios	scVEGF/Cy	IS750	Ratios	scVEGF/Cy	IS750	scVEGF/Cy	IS750
Tumor/Tissue	2.98	3.71	Margin/Center	5.81	−1.25	5.37	−9.94
Tumor/Bones	1.68	3.57	Margin/Tissue	8.46	4.90	20.78	10.11
			Center/Tissue	2.65	6.15	15.41	20.06

Fig. 4 Reconstruction of LLC mouse model and coregistration of FMT-XCT-PET. (a) *In vivo* reconstruction of IntegriSense680 (orange) and overlay of FDG-PET reconstruction (green). The green arrow highlights a region where the PET reconstruction indicates higher FDG uptake. FMT reconstruction in the same area does not show any fluorescence signal. (b) *Ex vivo* validation slice of IntegriSense 680 fluorescence (orange). The fluorescence image was enhanced for better contrast. (c) 3-D representation of both FMT (orange) and PET (green) reconstructions. Orange arrows point to the FDG tumors as reconstructed by FMT and PET. The green arrow points to a third region of increased FDG uptake. (d) 3-D rendering of mouse skin and highlighted tumor areas (arrows). (e) Intensity profiles through the white dashed lines in (a) and (b) of *ex vivo* IntegriSense680 (orange), *in vivo* IntegriSense680 (yellow), and [^{18}F]-FDG (green) for line 1 (continuous) and line 2 (dashed), respectively. (3-D rendering was implemented using AMIRA software).

for 360-deg FMT data, to a limited-projection-angle implementation. The particular challenge, herein, was to identify on whether the regularization parameters are wavelength dependent and then on overall developing a methodology for automatic computation of regularization factors which would be optimal for limited-projection-angle FMT reconstructions. A next aim of the proposal was to offer the first co-registration of PET-FMT-XCT hybrid data, based on limited-projection-angle FMT reconstructions using priors.

The study defined a data-driven method based on two-step inversion for the application of prior knowledge to the reconstruction of limited-projection-angle hybrid FMT-XCT images. The first step was based on the computation of the mean reconstructed fluorescence strength per segment after Tikhonov reconstruction. The resulting regularization factors were subsequently used to guide the second inversion step.

We first investigated the influence of different regularization parameters λ on the automatic computation of regularization factors in a phantom. Although the effect of surface weighting was reduced with increasing values of λ [Fig. 1(a)], the increase in λ values also resulted in changed regularization factors, especially for λ values that were larger than λ_3, as evinced by the steep rise of the regularization factor curve in Fig. 1(c). This affected the contrast and localization of the fluorescence signal after step 2 inversion, which both decreased with increasing λ. According to these results, we considered a regularization with $\lambda_3 \approx 4 \cdot \lambda_1$, with λ_1 being the λ-value found at the corner of the L-curve calculated for the step 1 regularization. This proved to be a good compromise between high surface weighting and overregularization. We then confirmed this finding by applying our method to different mouse models, containing deep-seated tumors and superficial tumors. For both imaging studies carried out, individual channel specific regularization factors were found using λ_3. *In vivo* reconstruction results using this prior knowledge correlated with the validation from *ex vivo* cryosections, both in respect to signal localization and relative contrast.

Previously acquired data from lung imaging studies in Kras mice employing IntegriSense[21,25] were consulted to validate the regularization factors employed, herein. IntegriSense was shown in these studies to label tumors in the lung. Imaging within the lung requires regularization factors of lower value than the regularization factors of surrounding tissues. Such lower factors were only obtained in our current study using λ_3. The data-driven approach presented, herein, can therefore replace the manual selection of regularization factors and may provide user-independent and therefore possibly unbiased reconstructions.

Finally, we demonstrated how the combination of a different molecular imaging modality, i.e., PET, can also be employed to offer complementary information into different molecular processes. This approach takes advantage of particular strengths that each imaging modality may have, especially in regard to the availability of different agents that complement the ability to label desired targets. In this particular study, we observed on the one hand that PET reliably reconstructs the tumor location while FMT results exhibit a slight displacement between reconstruction and *ex vivo* validation. On the other hand, the uptake of [^{18}F]-FDG in nondiseased tissue can complicate the distinction of tumors from normal tissue. In this context, FMT was capable of contributing important information to this study since it reliably enabled the assessment of the number of tumors. Nevertheless, both modalities were able to reconstruct one large and one smaller tumor, in agreement with the injected cell number and cryosection results. Thus, the combination of PET and FMT in this case provided complementary information on the mouse model. An obvious further extension would be the integration of MRI data and the exploitation of its anatomical and functional imaging properties in combination with the molecular and anatomical data provided by limited-projection-angle FMT, PET, and XCT.

Labeling and imaging multiple biological entities enable simultaneous investigation of different tissues and organs, or

tracking of several cell populations, therefore enhancing insight into cell and developmental biology, cancer studies, and biomedicine.[29] Although findings based on *in vitro* and *ex vivo* approaches help in understanding the fundamental roles of different molecules in diseases or healing processes, *in vivo* tools can deepen the understanding of enzymatic activation and protein regulation in time-dependent cellular and molecular events. Simultaneous acquisition of multiple key features improves, hence, the understanding of such processes[40] or the characterization of cancer types[41–43] and facilitates the development of efficient drugs and therapies.

Taking advantage of the spectral potential of optical imaging methods and in particular of the *in vivo* imaging capabilities of FMT is, therefore, of predominant importance. The potential of FMT to perform tomographic imaging in planar geometry renders it furthermore a flexible and fast multimodality compatible device. We showed and discussed, herein, that hybrid limited-projection-angle FMT reconstructions are suitable for independent assessment of different spectral signatures in the same animal and can, hence, be used for multispectral studies, or multiparametric investigations in combination with other imaging modalities. Thus, complementary data can be gathered and an information-rich experimental environment is created.[26,40,44,45] The reduced acquisition times and the coregistration potential to basically any other *in vivo* imaging device provided by the imaging cartridge, make limited-projection-angle FMT particularly interesting for such multiparameter studies. Our approach of adapting automatic regularization factor computation to limited-projection-angle FMT is all the more important, the more manual factor selection is likely to bias the outcome of the reconstruction. This is particularly relevant for studies employing multiple fluorochromes in the same animal. In this context, anatomical data always stays unchanged while the fluorescence distribution differs depending on the used probe at each wavelength. Therefore, applying the same regularization factors for reconstructing all wavelengths may be wrong, since the different fluorochromes may distribute differently. Manually selecting different factors per wavelength could, on the other hand, introduce bias.

Beyond the investigation of multiple molecules, alternative dual-wavelength approaches aim at improving the quantification of fluorescence expression by separation of probe uptake and target presence[6] in epi-illumination imaging. In this example, one wavelength was used to establish an internal control by providing a background measurement by an untargeted fluorescence probe. Similarly, such a concept was recently applied to FMT (Ref. [7]) and showed the improved reconstruction of fluorescence localization. In order to move toward absolute quantification in contrast to relative quantification as presented herein, as well as improved localization, the adaptation of such internal control methods could further enhance multiparameter FMT methods, particularly in regard to longitudinal studies where the measurements at different time points should be quantitatively comparable. One untargeted probe could consequently be used to normalize many other functional probes. Due to the wavelength-independent nature of our hybrid method, an extension of our concept to measuring more than two probes would suggest itself. Hence, accurate and quantitative reconstructions of many fluorescence molecules could be achieved.

Several limitations are present in this study. Slight discrepancies in tumor localization still exist and were observed in this study in mice containing more than one tumor (Kras and LLC).

The fluorescence emission from multiple locations, hence, still affects accurate reconstruction. Additionally, broadly distributed fluorescence, as exhibited by AngioSense in the Kras model, was less consistently recovered than the localized signal from IntegriSense, as shown in the intensity profile in Fig. 2(d). The distinction of signal from background in such cases seems less reliable. Several approaches to account for these limitations are conceivable. Using contrast agents for XCT or employing MRI as anatomical imaging modality could improve the segmentation of tumor tissue and hence directly influence the FMT reconstruction in terms of localization. More importantly, localization as well as quantification and background detection issues could be resolved by adapting the previously proposed internal control method.

To conclude, the automatic computation of regularization factors for *a priori* reconstruction enables simultaneous but independent investigation of multiple molecules and accurate comparison and combination of limited-projection-angle FMT with other molecular imaging devices. This is of utmost importance for the realistic assessment of any disease, since multiple molecules play a role in their progression and therapy. Such *in vivo*, noninvasive, and multiparameter investigations can significantly improve the understanding of dynamic processes because the same animal can be imaged over longer time periods and information is gathered from the most realistic experimental setup possible—the living organism. Last but not least, such multiple dynamic readings could be employed beyond traditional biological investigations to computational models of diseases and systems biology applications.

References

1. V. Ntziachristos et al., "Looking and listening to light: the evolution of whole-body photonic imaging," *Nat. Biotechnol.* **23**(3), 313–320 (2005).
2. R. Weissleder and M. J. Pittet, "Imaging in the era of molecular oncology," *Nature* **452**(7187), 580–589 (2008).
3. R. Weissleder, "Scaling down imaging: molecular mapping of cancer in mice," *Nat. Rev. Cancer* **2**(1), 11–18 (2002).
4. B. Ballou et al., "Tumor labeling in vivo using cyanine-conjugated monoclonal antibodies," *Cancer Immunol. Immunother.* **41**(4), 257–263 (1995).
5. U. Mahmood and R. Weissleder, "Near-infrared optical imaging of proteases in cancer," *Mol. Cancer Ther.* **2**(5), 489–496 (2003).
6. J. Baeten et al., "*In vivo* investigation of breast cancer progression by use of an internal control," *Neoplasia* **11**(3), 220–227 (2009).
7. K. M. Tichauer et al., "Dual-tracer background subtraction approach for fluorescent molecular tomography," *J. Biomed. Opt.* **18**(1), 016003 (2013).
8. R. L. Barbour et al., "MRI-guided optical tomography: prospects and computation for a new imaging method," *IEEE Comput. Sci. Eng.* **2**(4), 63–77 (1995).
9. S. R. Arridge and J. C. Hebden, "Optical imaging in medicine: II. Modelling and reconstruction," *Phys. Med. Biol.* **42**(5), 841–853 (1997).
10. S. R. Arridge, "Optical tomography in medical imaging," *Inverse Probl.* **15**(2), R41–R93 (1999).
11. A. N. Tikhonov and V. Y. Arsenin, *Solutions of Ill-Posed Problems*, John Wiley & Sons, New York (1977).

12. J. Haller et al., "Visualization of pulmonary inflammation using non-invasive fluorescence molecular imaging," *J. Appl. Physiol.* **104**(3), 795–802 (2008).
13. X. Intes et al., "Diffuse optical tomography with physiological and spatial a priori constraints," *Phys. Med. Biol.* **49**(12), N155–N163 (2004).
14. P. K. Yalavarthy et al., "Structural information within regularization matrices improves near infrared diffuse optical tomography," *Opt. Express* **15**(13), 8043–8058 (2007).
15. S. C. Davis et al., "Image-guided diffuse optical fluorescence tomography implemented with Laplacian-type regularization," *Opt. Express* **15**(7), 4066–4082 (2007).
16. D. Hyde et al., "Hybrid FMT-CT imaging of amyloid-beta plaques in a murine Alzheimer's disease model," *Neuroimage* **44**(4), 1304–1311 (2009).
17. Y. Lin et al., "Quantitative fluorescence tomography with functional and structural a priori information," *Appl. Opt.* **48**(7), 1328–1336 (2009).
18. D. Hyde et al., "Performance dependence of hybrid x-ray computed tomography/fluorescence molecular tomography on the optical forward problem," *J. Opt. Soc. Am. A* **26**(4), 919–923 (2009).
19. T. Pyka et al., "Revisiting the normalized Born approximation: effects of scattering," *Opt. Lett.* **36**(22), 4329–4331 (2011).
20. A. Ale et al., "Imaging performance of a hybrid x-ray computed tomography-fluorescence molecular tomography system using priors," *Med. Phys.* **37**(5), 1976–1986 (2010).
21. A. Ale et al., "FMT-XCT: in vivo animal studies with hybrid fluorescence molecular tomography-X-ray computed tomography," *Nat. Methods* **9**(6), 615–620 (2012).
22. R. B. Schulz et al., "Hybrid system for simultaneous fluorescence and x-ray computed tomography," *IEEE Trans. Med. Imaging* **29**(2), 465–473 (2010).
23. X. Yang et al., "Combined system of fluorescence diffuse optical tomography and microcomputed tomography for small animal imaging," *Rev. Sci. Instrum.* **81**(5), 054304 (2010).
24. A. Da Silva et al., "Optical calibration protocol for an x-ray and optical multimodality tomography system dedicated to small-animal examination," *Appl. Opt.* **48**(10), D151–D162 (2009).
25. K. Radrich et al., "Improving limited-projection-angle fluorescence molecular tomography using a co-registered x-ray computed tomography scan," *J. Biomed. Opt.* **17**(12), 126011 (2012).
26. S. C. Davis et al., "Dynamic dual-tracer MRI-guided fluorescence tomography to quantify receptor density in vivo," *Proc. Natl. Acad. Sci. U. S. A.* **110**(22), 9025–9030 (2013).
27. J. Livet et al., "Transgenic strategies for combinatorial expression of fluorescent proteins in the nervous system," *Nature* **450**(7166), 56–62 (2007).
28. R. M. Levenson et al., "Multiplexing with multispectral imaging: from mice to microscopy," *ILAR J* **49**(1), 78–88 (2008).
29. D. M. Shcherbakova and V. V. Verkhusha, "Near-infrared fluorescent proteins for multicolor *in vivo* imaging," *Nat. Methods* **10**(8), 751–754 (2013).
30. X. Gao et al., "In vivo cancer targeting and imaging with semiconductor quantum dots," *Nat. Biotechnol.* **22**(8), 969–976 (2004).
31. D. Hyde et al., "Data specific spatially varying regularization for multimodal fluorescence molecular tomography," *IEEE Trans. Med. Imaging* **29**(2), 365–374 (2010).
32. M. Freyer et al., "Fast automatic segmentation of anatomical structures in x-ray computed tomography images to improve fluorescence molecular tomography reconstruction," *J. Biomed. Opt.* **15**(3), 036006 (2010).
33. T. Lasser and V. Ntziachristos, "Optimization of 360 degrees projection fluorescence molecular tomography," *Med. Image Anal.* **11**(4), 389–399 (2007).
34. E. E. Graves et al., "A submillimeter resolution fluorescence molecular imaging system for small animal imaging," *Med. Phys.* **30**(5), 901–911 (2003).
35. P. C. Hansen, "Analysis of discrete ill-posed problems by means of the L-curve," *SIAM Rev.* **34**(4), 561–580 (1992).
36. L. Johnson et al., "Somatic activation of the K-ras oncogene causes early onset lung cancer in mice," *Nature* **410**(6832), 1111–1116 (2001).
37. A. Sarantopoulos, G. Themelis, and V. Ntziachristos, "Imaging the bio-distribution of fluorescent probes using multispectral epi-illumination cryoslicing imaging," *Mol. Imaging Biol.* **13**(5), 874–885 (2010).
38. A. Ale et al., "Cardioprotective C-kit(+) bone marrow cells attenuate apoptosis after acute myocardial infarction in mice—in vivo assessment with fluorescence molecular imaging," *Theranostics* **3**(11), 903–913 (2013).
39. A. Taruttis et al., "Multispectral optoacoustic tomography of myocardial infarction," *Photoacoustics* **1**(1), 3–8 (2013).
40. M. Nahrendorf et al., "Dual channel optical tomographic imaging of leukocyte recruitment and protease activity in the healing myocardial infarct," *Circ. Res.* **100**(8), 1218–1225 (2007).
41. H. Kobayashi et al., "Rational chemical design of the next generation of molecular imaging probes based on physics and biology: mixing modalities, colors and signals," *Chem. Soc. Rev.* **40**(9), 4626–4648 (2011).
42. H. Kobayashi et al., "Multiplexed imaging in cancer diagnosis: applications and future advances," *Lancet Oncol.* **11**(6), 589–595 (2010).
43. Y. Koyama et al., "In vivo molecular imaging to diagnose and subtype tumors through receptor-targeted optically labeled monoclonal antibodies," *Neoplasia* **9**(12), 1021–1029 (2007).
44. M. Solomon et al., "Multimodal fluorescence-mediated tomography and SPECT/CT for small-animal imaging," *J. Nucl. Med.* **54**(4), 639–646 (2013).
45. M. Nahrendorf et al., "Hybrid PET-optical imaging using targeted probes," *Proc. Natl. Acad. Sci. U. S. A.* **107**(17), 7910–7915 (2010).

Karin Radrich received a Dipl-Ing and MSc in electrical engineering within the scope for a double degree program from Technische Universität München and Ecole Centrale Paris in 2009. She is currently pursuing her PhD at the Institute for Biological and Medical Imaging (IBMI) at Technische Universität München and Helmholtz Zentrum München under guidance of Prof. Vasilis Ntziachristos. Her research focuses on fluorescence molecular tomography and multispectral imaging for *in-vivo* biomedical imaging applications.

Pouyan Mohajerani received a BS degree in electrical engineering from Sharif University of Technology in Tehran, Iran. He later received his MSc in electrical engineering in 2004 from Georgia Institute of Technology, Atlanta. He is currently a PhD student in the Institute for Biological and Medical Imaging at Technische Universität München and Helmholtz Zentrum München, Munich, Germany. His current research interests are fluorescence tomography, inverse problems, molecular imaging, signal processing and musculoskeletal imaging.

Johanna Bussemer studied biology at the Technical University Munich and the University of Michigan. She received her PhD in the field of cell biology from the Ludwig-Maximilian-University Munich. Her current research at the Department of Nuclear Medicine at the University hospital of the TUM focuses on the application of PET/CT and MRI imaging to evaluate novel anti-cancer therapeutics for the treatment of mammary carcinoma.

Markus Schwaiger, MD, received his medical training at the Medical School of the FU Berlin and completed a fellowship at the division of nuclear medicine, UCLA School of Medicine, Los Angeles. There he served as assistant professor of radiological sciences. Subsequently he served as professor of medicine, division of nuclear medicine, University of Michigan. He is currently professor and director, department of nuclear medicine, TUM. His research focuses on molecular imaging in cardiology and oncology.

Vasilis Ntziachristos holds a professorial Chair of Biological Imaging at the Technische Universität München and is director of the Institute for Biological and Medical Imaging at the Helmholtz Zentrum München. His research encompasses the development of new methods and devices for biological and medical imaging. Focusing on innovative, noninvasive approaches that visualize previously unseen physiological and molecular processes in tissues, he aims to offer new, efficient methods for diagnostics and theranostics.

Ambros J. Beer: Biography is not available.